Robust Protection from Backscattering in the Topological Insulator $Bi_{1.5}Sb_{0.5}Te_{1.7}Se_{1.3}$

Sunghun Kim,[1,*] Shunsuke Yoshizawa,[1] Yukiaki Ishida,[1] Kazuma Eto,[2] Kouji Segawa,[2] Yoichi Ando,[2,†] Shik Shin,[1] and Fumio Komori[1,‡]

[1]*Institute for Solid State Physics, The University of Tokyo, Kashiwa, Chiba 277-8581, Japan*

[2]*Institute of Scientific and Industrial Research, Osaka University, Ibaraki, Osaka 567-0047, Japan*

(Received 11 October 2013; published 1 April 2014)

Electron scattering in the topological surface state (TSS) of the topological insulator $Bi_{1.5}Sb_{0.5}Te_{1.7}Se_{1.3}$ was studied using quasiparticle interference observed by scanning tunneling microscopy. It was found that not only the 180° backscattering but also a wide range of backscattering angles of 100°–180° are effectively prohibited in the TSS. This conclusion was obtained by comparing the observed scattering vectors with the diameters of the constant-energy contours of the TSS, which were measured for both occupied and unoccupied states using time- and angle-resolved photoemission spectroscopy. The robust protection from backscattering in the TSS is good news for applications, but it poses a challenge to the theoretical understanding of the transport in the TSS.

DOI: 10.1103/PhysRevLett.112.136802 PACS numbers: 73.20.-r, 68.37.Ef, 78.47.da, 79.60.-i

Three-dimensional topological insulators (TIs) are accompanied by gapless surface states due to a nontrivial Z_2 topology of the bulk wave functions [1–3]. Such a topological surface state (TSS) of a 3D TI is peculiar in that it is helically spin polarized, which leads to a suppression of electron scatterings due to spin mismatch between the eigenstates before and after the scattering [1,3]; in particular, 180° backscattering is expected to be absent, because $+\mathbf{k}$ and $-\mathbf{k}$ states have completely opposite spins. Such a protection of the TSS from backscattering has been elucidated to play a key role in maintaining a high mobility of the carriers in the TSS [4], and this characteristic is one of the reasons why TIs are an appealing platform for various device applications [5].

In STM experiments, the suppression of backscattering in TIs has been inferred from the measurements of quasiparticle interference (QPI) in $Bi_{1-x}Sb_x$ [6], Bi_2Te_3 [7,8], and Bi_2Se_3 [9], as well as in Ca- and Mn-doped Bi_2Te_3 and Bi_2Se_3 [10]. In $Bi_{1-x}Sb_x$, which has multiple surface bands, strong interference was observed only between those surface bands that have the same spin orientation. On the other hand, in Bi_2Te_3 and Bi_2Se_3, where the TSS consists of a single Dirac cone, no interference has been detected unless the Dirac cone becomes significantly warped at energies away from the Dirac point [7–11]; remember, in those materials a term proportional to $k^3\sigma_z$ describing the cubic spin-orbit coupling shows up in the effective Hamiltonian [12], which results in hexagonal warping of the Dirac cone that has been experimentally observed by angle-resolved photoemission spectroscopy (ARPES) [13,14].

In those previous experiments, the suppression of backscattering due to the helical spin polarization of the TSS was only qualitatively elucidated, because no QPI was observed for intraband scatterings in $Bi_{1-x}Sb_x$ nor for circular constant-energy contours of the TSS in Bi_2Te_3 and Bi_2Se_3. In other words, it has not been clear to what extent the backscattering is suppressed as a function of scattering angle when the scattering takes place within the same surface band whose constant-energy contour is not warped. Even though such information is crucial for establishing concrete understanding of the transport in the TSS, until recently no TI material has allowed us to observe QPI in an unwarped Dirac cone.

This situation has changed with the recent discovery of the TI material $Bi_{2-x}Sb_xTe_{3-y}Se_y$ [15,16]. This is the first TI material in which the surface-dominated transport was achieved in bulk single crystals [16], and the Fermi energy E_F can be tuned in the bulk band gap by changing the composition along particular combinations of (x, y) to realize the maximally charge-compensated state [15,17]. The alloyed nature of this material is expected to cause long-range potential fluctuations [6], which would lead to relatively strong scattering of long-wavelength electrons (i.e., Bloch electrons with small k), even though the surface carrier mobility is high enough to present clear Shubnikov–de Haas oscillations [16]. Indeed, a recent STM study of $Bi_{1.5}Sb_{0.5}Te_{1.7}Se_{1.3}$ found QPI to be observable [18] despite the weak warping of the Dirac cone. Therefore, $Bi_{2-x}Sb_xTe_{3-y}Se_y$ offers a promising platform for quantitatively understanding one of the most important characteristics of TIs, the suppression of backscattering, in a nearly ideal Dirac cone.

In this Letter, we elucidate how the elastic scattering among the helically spin-polarized surface electrons of $Bi_{1.5}Sb_{0.5}Te_{1.7}Se_{1.3}$ is suppressed as a function of the scattering angle and electron energy in the unwarped portion of the Dirac cone. Such information became available because elastic scattering of electrons manifests itself in the QPI down to energies close to the Dirac-point energy E_D, thanks to the long-range potential fluctuations

in this material. We found that there is a sharp threshold for the length of the scattering vector, above which the QPI intensity is abruptly diminished. Such a threshold points to the existence of a well-defined critical scattering angle beyond which elastic scattering is suddenly suppressed. By comparing the length of the critical scattering vector in the QPI with the diameters of the constant-energy contours of the TSS, we found that the maximum scattering angle is $\sim 100°$ and is independent of the energy location, as long as the bulk scattering channel does not intervene. For this comparison, we measured the dispersions of the unoccupied states by using time-resolved ARPES (TrARPES) implementing a pump-probe method, because in this material E_F is located very close to E_D and a major part of the upper Dirac cone is unmeasurable with usual ARPES.

The single crystals of $Bi_{1.5}Sb_{0.5}Te_{1.7}Se_{1.3}$ were grown by melting stoichiometric mixtures of high-purity elements in sealed quartz tubes as described in Ref. [15]. The crystal structure was confirmed by x-ray diffraction. Experiments using STM and TrARPES were performed in two separated UHV systems. After a clean surface was prepared by cleaving the crystal in UHV of better than 2×10^{-8} Pa at room temperature, the sample was transferred *in situ* in UHV either to the cooled stage in the STM chamber or to the TrARPES chamber.

The STM images and tunneling spectra were taken at 5 K using a cryogenic STM with an electrochemically etched W tip. The tip apex and its metallic density of states were checked by scanning a clean Pt(111) surface. Topographic images were obtained using a constant-current mode. For the study of QPI, differential-conductance (dI/dV) spectroscopy was performed using a standard lock-in technique with a bias-voltage modulation of $5 - 10$ mV_{rms} at 496 Hz. The dI/dV curve was measured at every point of a 256×256 grid on the surface. The obtained data were plotted as a function of position to make a dI/dV map. The constant-energy dI/dV maps were Fourier transformed (FT), and the peaks due to the surface lattice were used for the calibration of the wave-vector space. The FT patterns were symmetrized with respect to the sixfold symmetry, on the basis of the C_{3v} symmetry of the cleaved surface.

In the TrARPES experiments, we used 1.5 eV (pump) and 5.9 eV (probe) pulsed photons from an amplified Ti: sapphire laser system with repetition rate of 250 kHz [19]. The pulse widths were 170 and 250 fs and the spot diameters were ~ 0.4 and ~ 0.2 mm for the 1.5 and 5.9 eV photons, respectively. The time delay between the pump and the probe pulses was optimized to clarify the unoccupied TSS band in the bulk band gap [20]. Photoelectrons from the cleaved surface cooled to 5 K were detected by a hemispherical analyzer. The energy resolution of the photoelectrons was 15 meV.

Typical STM images of the cleaved surface at 5 K are shown in Figs. 1(a) and 1(b). In the magnified image, surface atoms are recognized with a distribution of the apparent height. The $Bi_{1.5}Sb_{0.5}Te_{1.7}Se_{1.3}$ crystal consists of quintuple-layer units of (Te/Se)-(Bi/Sb)-Se-(Bi/Sb)-(Te/Se) that are stacked and weakly bonded by the van der Waals force, as schematically shown in Fig. 1(c). The cleavage occurs along the van der Waals gap, and the flat cleaved surface is always the Te/Se layer. The local density of states fluctuates because of the inhomogeneous distributions of Te and Se, as well as those of Bi and Sb, in the crystal. Thus, the observed distribution of the apparent height of the surface atoms is attributed to the electronic effect due to the alloying in the Bi/Sb and Te/Se layers.

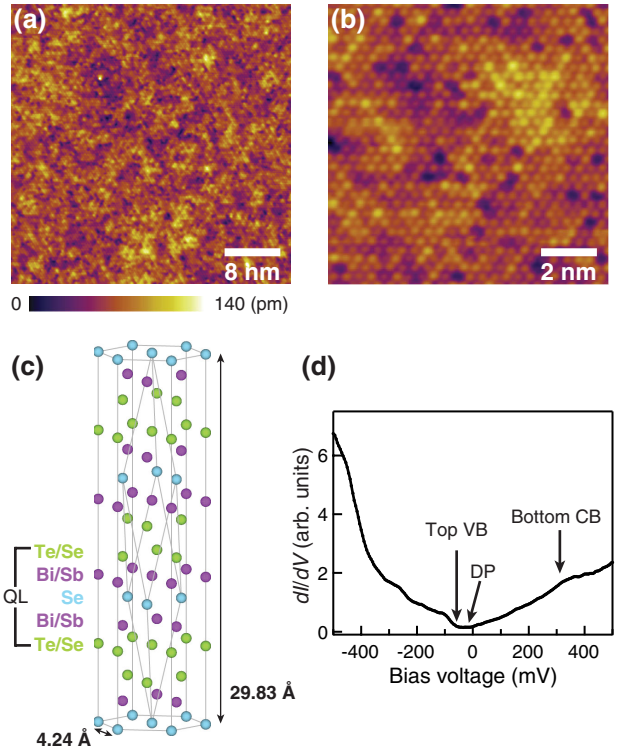

FIG. 1 (color online). (a),(b) STM images of a cleaved surface of $Bi_{1.5}Sb_{0.5}Te_{1.7}Se_{1.3}$. Protrusions are Te or Se atoms at the surface. The density of surface point defects is less than 3%. The sample bias voltage and tunneling current were -0.4 V and 20 pA in (a) and -0.6 V and 100 pA in (b). (c) Crystal structure of $Bi_{1.5}Sb_{0.5}Te_{1.7}Se_{1.3}$. (d) Typical differential-conductance curve measured on a cleaved surface at 5 K. The positions of the top of the bulk valence band, the Dirac point, and the bottom of the bulk conduction band are marked by arrows. The latter is known from the result of TrARPES.

An example of the point tunneling spectrum is shown in Fig. 1(d). The Dirac-point energy E_D can be defined as the minimum in dI/dV and varies over the surface (the variation of the point spectra and the distribution of E_D are shown in Ref. [21]). The average location of E_D is 10 ± 15 meV below E_F. In the point tunneling spectra [Fig. 1(d) and Ref. [21]], the differential conductance rapidly increases below E_D compared to that above E_D. This is because the top of the bulk valence band, which can

be recognized as a clear shoulder in the dI/dV curve in Fig. 1(d), is located just below E_D. The bottom of the bulk conduction band is, however, not very clear in the tunneling spectrum.

Figures 2(a) and 2(b) show dI/dV maps of the cleaved surface for two selected sample bias voltages V_B in the bulk band gap, and the corresponding FT images are shown in Figs. 2(c) and 2(d) [21]. The cross sections of the FT images at the two V_B values are shown in Figs. 2(e) and 2(f) for the two high-symmetry directions, $\bar{\Gamma}$-$\bar{K}$ and $\bar{\Gamma}$-$\bar{M}$. In each cross section, one notices a steep decrease of the scattering amplitude with increasing scattering-vector length q. Such a steep decrease in the scattering amplitude was observed in the V_B range of 60–300 mV. This range corresponds to the energy window where the TSS is located in the bulk band gap. Our data indicate that the electron scattering within the TSS is rapidly diminished when the scattering-vector length exceeds a certain critical value. Hence, we call it critical scattering-vector length and denote it q_{cx} and q_{cy} for $\bar{\Gamma}$-$\bar{K}$ and $\bar{\Gamma}$-$\bar{M}$ directions, respectively. Obviously, they both increase with increasing V_B; to substantiate this trend, the FT amplitudes in the $\bar{\Gamma}$-$\bar{K}$ and $\bar{\Gamma}$-$\bar{M}$ directions are shown in Fig. 2(g) as an image on the scattering-vector length q versus V_B plane, and the critical scattering-vector lengths are marked by red and blue symbols on the image. The critical lengths increase with increasing energy, and the slope is reproducible in other regions of the surface [21].

To quantitatively understand the implications of the observed critical scattering-vector lengths, information regarding the TSS dispersion above E_F is important. Such information is unavailable with the ordinary ARPES, but the TrARPES makes it possible to measure it with a high resolution. To demonstrate the power of TrARPES, Figs. 3(a) and 3(b) compare the results of TrARPES at 5 K before and after filling the unoccupied side by the pump-induced electrons. The cut is along the $\bar{\Gamma}$-$\bar{K}$ direction. The band dispersion of the TSS was observed up to 0.25 eV above E_F, as shown in Fig. 3(b); the unoccupied states at

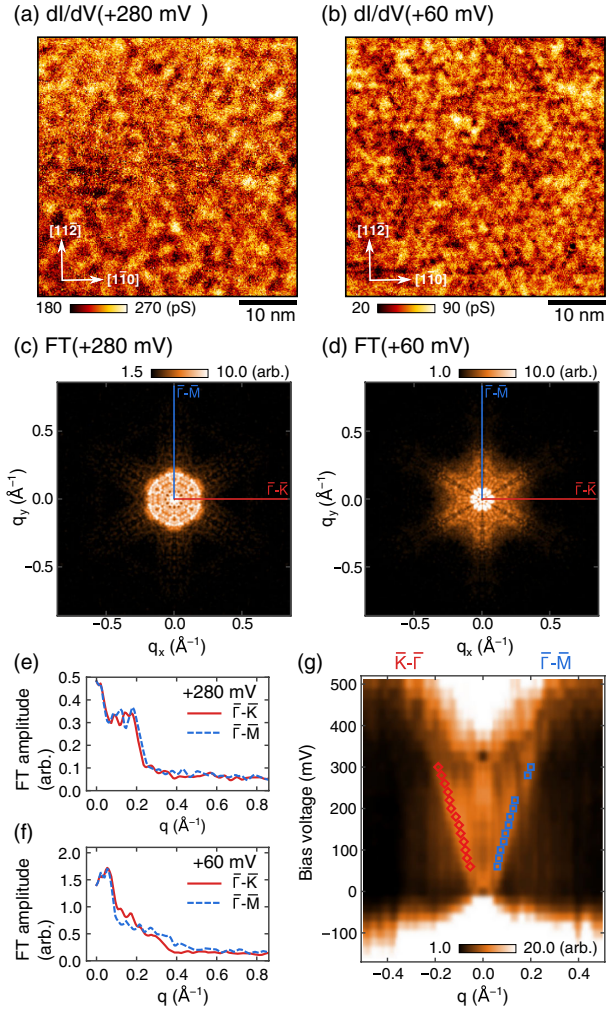

FIG. 2 (color online). (a),(b) Differential-conductance images of the cleaved surface for V_B of (a) 280 mV and (b) 60 mV in the bulk band gap. (c),(d) Corresponding FT amplitude images. (e), (f) Cross sections of the FT amplitude for the images (c) and (d), respectively. The results in the $\bar{\Gamma}$-$\bar{K}$ (solid red line) and $\bar{\Gamma}$-$\bar{M}$ (dotted blue line) directions are shown. (g) FT amplitude images as functions of V_B and the scattering-vector length q in the $\bar{\Gamma}$-$\bar{K}$ (left) and $\bar{\Gamma}$-$\bar{M}$ (right) directions. Diamond (red) and square (blue) symbols indicate the critical scattering-vector lengths in the two directions.

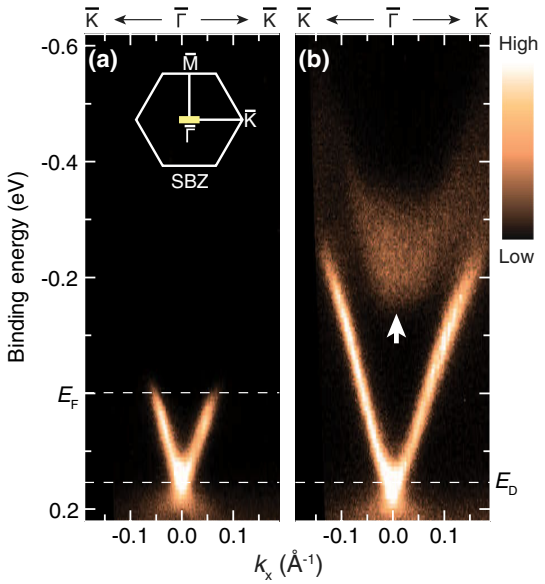

FIG. 3 (color online). (a),(b) Photoemission intensity images of the cleaved surface of $Bi_{1.5}Sb_{0.5}Te_{1.7}Se_{1.3}$ plotted along the $\bar{\Gamma}$-$\bar{K}$ direction; images (a) and (b) were obtained before (−0.8 ps) and after (+1.1 ps) filling the unoccupied states with the 1.5 eV pump photons, respectively. Dispersions above the Fermi level became visible by pumping electrons into the unoccupied side. The bottom of the unoccupied bulk conduction band is indicated by an arrow. The inset of (a) shows the surface Brillouin zone, together with the range covered by the TrARPES measurements shown as a short thick line.

the center of the surface Brillouin zone in this figure are naturally assigned to the bulk states, on the basis of the electronic states of Bi_2Te_3 and Bi_2Se_3 [13,14]. The band shape [21] of the TSS shown in Fig. 3(a) is consistent with the previous result [17]. Judging from the spectrum width, the distribution of E_D over the measured region is as narrow as that estimated by the dI/dV maps [21]. We note that E_D in those ARPES data is located at 0.15 eV below E_F, which is lower than that observed in the tunneling spectrum shown in Fig. 1(d). This difference can be explained by the electron doping from adsorbates such as hydrogen that often occurs during ARPES measurements at low temperature [22]. In spite of the shift of E_D, the band velocity of TSS remains the same, so that it does not affect the discussions hereafter [21].

The velocity of the surface band was obtained by analyzing the momentum distribution curves [21], and is 4.9×10^5 m/s for $E - E_D > 80$ meV. Below that energy, it decreases as in the previous reports [3,23,24] on Bi_2Se_3. No significant difference in the band dispersion was observed between the $\bar{\Gamma}$-$\bar{M}$ and $\bar{\Gamma}$-$\bar{K}$ directions by TrARPES for energies up to 100 meV above E_F within our experimental accuracy. This means that the cross section of the TSS is close to circular in this energy range, and warping would become noticeable only at higher energies.

Knowing the TSS dispersion above E_F for $Bi_{1.5}Sb_{0.5}Te_{1.7}Se_{1.3}$, we are now in the position to make quantitative analysis of the critical scattering-vector lengths found in the QPI data. In Fig. 4(a), q_{cx} and q_{cy} are compared with the diameter of the cross section of the Dirac cone TSS observed by TrARPES. Here, the origin of the energy is commonly set to be E_D. The critical scattering-vector lengths is about 75% of the corresponding diameter of the TSS at any energy between 90 and 310 meV above E_D. Note that if scattering is allowed for the scattering angle θ, of up to 180° (i.e., no restriction for backscattering), q_c should be equal to the diameter of the TSS. Hence, the fact that q_c is limited to 75% of the diameter of the TSS means that the allowed scattering angle has a maximum, which can be easily calculated to be 100°. This situation is schematically depicted in Figs. 4(c) and 4(d) for circular and warped cross sections of the TSS. Figure 4(b) graphically shows that this maximum scattering angle does not change with energy. This result indicates that not only the 180° backscattering but also a rather wide range of backscattering angle of 100°–180° are effectively prohibited due to the spin mismatch between the initial and final states in the TSS. This is good news for applications to utilize the protection of the TSS from backscattering.

The spin-mismatch mechanism for the present helical-spin system introduces an angle-dependent factor to the scattering probability. This factor is given [25] as $1 + \cos\theta$. The probability decreases rapidly with increasing θ for $\theta \gtrsim 90°$, and completely vanishes at $\theta = 180°$; this explains the strong suppression of scatterings for a relatively wide range of the scattering angle, at least qualitatively.

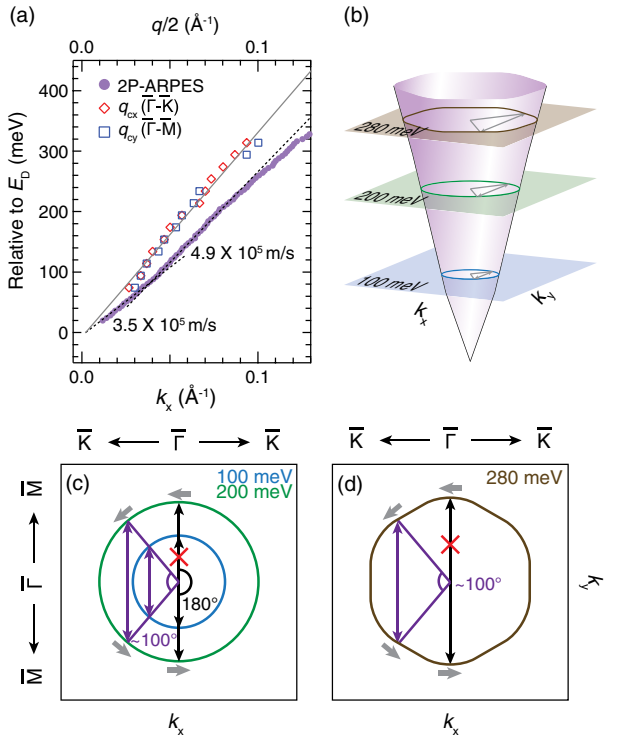

FIG. 4 (color online). (a) The critical scattering-vector lengths q_{cx} and q_{cy} and the diameter of constant-energy contour of the TSS are plotted for various energies from E_D to $E_D + 310$ meV; q_{cx} and q_{cy} were obtained from Fig. 2(g), and the diameter of the TSS in the $\bar{\Gamma}$-$\bar{K}$ direction was calculated from Fig. 3(b). (b) Schematic picture of the energy-dependent shape of the upper Dirac cone together with the available scattering vectors at representative energies. (c),(d) Schematic pictures for circular and warped TSS, respectively, to indicate that the critical scattering-vector lengths being 75% of the diameter of TSS corresponds to the maximum scattering angle of 100°; any scattering with a larger angle requires longer scattering vectors and hence is prohibited.

Naturally, further theoretical study including the realistic scattering potential in the present TSS is strongly called for to account for this robust protection from backscattering.

In summary, we found critical scattering-vector lengths in the QPI, beyond which elastic scattering of electrons in the TSS is significantly suppressed. The comparison with the TSS dispersions for the unoccupied states obtained from TrARPES allowed us to conclude that the protection from backscattering in the TSS occurs not only for 180° but also for a rather wide range of angles of 100°–180°. Also, such a wide angle range for the protection from backscattering is found to be essentially independent of the energy until the Dirac cone becomes warped and/or the bulk scattering events intervene. At energies higher than 300 meV, we found hexagonal patterns in the FT-QPI images that come from warping of the Dirac cone, and in this energy range the critical scattering vector was not clearly observed, indicating a different mechanism of the protection from backscattering in the warped Dirac cone.

The authors thank Y. Ozawa and T. Otsu for their improvement in the TrARPES measurements. This work was partly supported by JSPS (KAKENHI No. 21244048 and No. 25220708, and FIRST program), MEXT (Innovative Area "Topological Quantum Phenomena" KAKENHI), and AFOSR (AOARD 124038).

*kimsh@issp.u-tokyo.ac.jp
†y_ando@sanken.osaka-u.ac.jp
‡komori@issp.u-tokyo.ac.jp

[1] M. Z . Hasan and C. L. Kane, Rev. Mod. Phys. **82**, 3045 (2010).
[2] X.-L. Qi and S.-C. Zhang, Rev. Mod. Phys. **83**, 1057 (2011).
[3] Y. Ando, J. Phys. Soc. Jpn. **82**, 102001 (2013).
[4] A. A. Taskin, S. Sasaki, K. Segawa, and Y. Ando, Phys. Rev. Lett. **109**, 066803 (2012).
[5] J. E. Moore, Nature (London) **464**, 194 (2010).
[6] P. Roushan, J. Seo, C. V. Parker, Y. S. Hor, D. Hsieh, D. Qian, A. Richardella, M. Z. Hasan, R. J. Cava, and A. Yazdani, Nature (London) **460**, 1106 (2009).
[7] T. Zhang, P. Cheng, X. Chen, J.-F. Jia, X. Ma, K. He, L. Wang, H. Zhang, X. Dai, Z. Fang, X. Xie, and Q.-K. Xue, Phys. Rev. Lett. **103**, 266803 (2009).
[8] Z. Alpichshev, J. G. Analytis, J.-H. Chu, I. R. Fisher, Y. L. Chen, Z. X. Shen, A. Fang, and A. Kapitulnik, Phys. Rev. Lett. **104**, 016401 (2010).
[9] T. Hanaguri, K. Igarashi, M. Kawamura, H. Takagi, and T. Sasagawa, Phys. Rev. B **82**, 081305 (2010).
[10] H. Beidenkopf, P. Roushan, J. Seo, L. Gorman, I. Drozdov, Y. S. Hor, R. J. Cava, and A. Yazdani, Nat. Phys. **7**, 939 (2011).
[11] X. Zhou, C. Fang, W.-F. Tsai, and J. P. Hu, Phys. Rev. B **80**, 245317 (2009).
[12] L. Fu, Phys. Rev. Lett. **103**, 266801 (2009).
[13] Y. L. Chen, J. G. Analytis, J.-H. Chu, Z. K. Liu, S.-K. Mo, X. L. Qi, H. J. Zhang, D. H. Lu, X. Dai, Z. Fang, S. C. Zhang, I. R. Fisher, Z. Hussain, and Z.-X. Shen, Science **325**, 178 (2009).
[14] K. Kuroda, M. Arita, K. Miyamoto, M. Ye, J. Jiang, A. Kimura, E. E. Krasovskii, E. V. Chulkov, H. Iwasawa, T. Okuda, K. Shimada, Y. Ueda, H. Namatame, and M. Taniguchi, Phys. Rev. Lett. **105**, 076802 (2010).
[15] Z. Ren, A. A. Taskin, S. Sasaki, K. Segawa, and Y. Ando, Phys. Rev. B **84**, 165311 (2011).
[16] A. A. Taskin, Z. Ren, S. Sasaki, K. Segawa, and Y. Ando, Phys. Rev. Lett. **107**, 016801 (2011).
[17] T. Arakane, T. Sato, S. Souma, K. Kosaka, K. Nakayama, M. Komatsu, T. Takahashi, Z. Ren, K. Segawa, and Y. Ando, Nat. Commun. **3**, 636 (2012).
[18] W. Ko, I. Jeon, H. W. Kim, H. Kwon, S.-J. Kahng, J. Park, J. S. Kim, S. W. Hwang, and H. Suh, Sci. Rep. **3**, 2656 (2013).
[19] Y. Ishida, T. Togashi, K. Yamamoto, M. Tanaka, T. Taniuchi, T. Kiss, M. Nakajima, T. Suemoto, and S. Shin, Sci. Rep. **1**, 64 (2011).
[20] J. A. Sobota, S. Yang, J. G. Analytis, Y. L. Chen, I. R. Fisher, P. S. Kirchmann, and Z.-X. Shen, Phys. Rev. Lett. **108**, 117403 (2012). Electrons are first excited by the pump pulse to the empty bands with the energy higher than that of the TSS band, and after the interband scattering, the TSS band is highly occupied with a certain delay time.
[21] See Supplemental Material at http://link.aps.org/supplemental/10.1103/PhysRevLett.112.136802 for additional STM images, spectra, and discussion on the artifacts in the FT images and on the TrARPES analyses.
[22] R. Jiang, L.-L. Wang, M. Huang, R. S. Dhaka, D. D. Johnson, T. A. Lograsso, and A. Kaminski, Phys. Rev. B **86**, 085112 (2012).
[23] Y. L. Chen, J.-H. Chu, J. G. Analytis, Z. K. Liu, K. Igarashi, H.-H. Kuo, X. L. Qi, S. K. Mo, R. G. Moore, D. H. Lu, M. Hashimoto, T. Sasagawa, S. C. Zhang, I. R. Fisher, Z. Hussain, and Z. X. Shen, Science **329**, 659 (2010).
[24] K. Kuroda, M. Ye, A. Kimura, S. V. Eremeev, E. E. Krasovskii, E. V. Chulkov, Y. Ueda, K. Miyamoto, T. Okuda, K. Shimada, H. Namatame, and M. Taniguchi, Phys. Rev. Lett. **105**, 146801 (2010).
[25] I. A. Nechaev, M. F. Jensen, E. D. L. Rienks, V. M. Silkin, P. M. Echenique, E. V. Chulkov, and P. Hofmann, Phys. Rev. B **80**, 113402 (2009).